ACS EARTH AND SPACE CHEMISTRY

http://pubs.acs.org/journal/aesccq

Article

Microbial Denitrification: Active Site and Reaction Path Models Predict New Isotopic Fingerprints

Jason D. Boettger,* Cajetan Neubauer, Sebastian H. Kopf, and James D. Kubicki

Cite This: *ACS Earth Space Chem.* 2022, 6, 2582−2594

Read Online

ACCESS | Metrics & More | Article Recommendations | Supporting Information

ABSTRACT: The study of isotopic fingerprints in nitrate ($\delta^{15}N$, $\delta^{18}O$, $\Delta^{17}O$) has enabled pivotal insights into the global nitrogen cycle and revealed new knowledge gaps. Measuring populations of isotopic homologs of intact NO_3^- ions (isotopologues) shows promise to advance the understanding of nitrogen cycling processes; however, we need new theory and predictions to guide laboratory experiments and field studies. We investigated the hypothesis that the isotopic composition of the residual nitrate pool is controlled by the N−O bond-breaking step in Nar dissimilatory nitrate reductase using molecular models of the enzyme active sites and associated kinetic isotope effects (KIEs). We integrated the molecular model results into reaction path models representing the reduction of nitrate under either closed-system or steady-state conditions. The predicted intrinsic KIE ($^{15}\varepsilon$ and $^{18}\varepsilon$) of the Nar active site matches observed fractionations in both culture and environmental studies. This is what would be expected if the isotopic composition of marine nitrate were controlled by dissimilatory nitrate reduction by Nar. For a closed system, the molecular models predict a pronounced negative $^{15}N-^{18}O$ clumping anomaly in residual nitrate. This signal could encode information about the amount of nitrate consumed in a closed system and thus constrain initial nitrate concentration and its isotopic composition. Similar clumped isotope anomalies can potentially be used to distinguish whether a system is open or closed to new nitrate addition. These mechanistic predictions can be tested and refined in combination with emerging ESI-Orbitrap measurements.

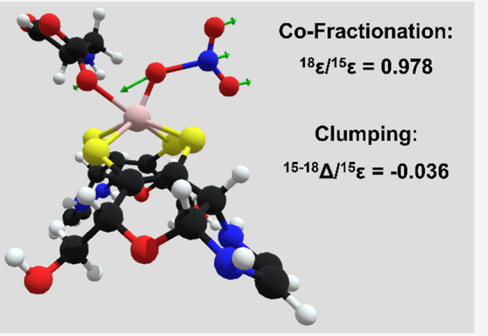

KEYWORDS: *isotope fractionation, clumped isotopes, nitrogen cycle, denitrification, molecular modeling, computational chemistry*

INTRODUCTION

Nitrate Reduction. Nitrogen is an essential element for organisms, integral to both amino acids and nucleic acids. Most N is inaccessible to organisms, locked in sedimentary deposits or in N_2 gas which is chemically inert. As a result, N is a limiting nutrient in many environments.[1] The nitrogen cycle converts N_2 gas into bioavailable forms such as NH_4^+ and NO_3^- and is primarily driven by microorganisms. The acceleration of anthropogenic nitrogen fertilizer production and use is upending long-evolved low-nutrient ecologies, with drastic impacts on biodiversity, eutrophication, and atmospheric pollution.[2]

The nitrogen cycle takes advantage of N's many available redox states ranging from −3 (in NH_4^+) to +5 (in NO_3^-). The change in redox state contributes to the large isotopic fractionations present in many steps of the nitrogen cycle.[3−9] The isotopic variability of N in the nitrogen cycle, and of the O bound to N in oxidized species, allows for stable isotopes to serve as a versatile tracer for its various synthesis and degradation processes.

The NO_3^- to NO_2^- reduction step is a key control on the ^{15}N and ^{18}O content of residual NO_3^-.[3] The $\delta^{15}N$ and $\delta^{18}O$ have been observed to covary in environmental NO_3^- samples in a regular way. The covariance can be described in terms of the $\delta^{18}O/\delta^{15}N$ slope of the environmental samples, or equivalently in terms of the $^{18}\varepsilon/^{15}\varepsilon$ slope of the NO_3^- reduction process itself, where ε refers to the apparent isotopic fractionation effect of the overall NO_3^- reduction reaction. In marine samples, the $\delta^{18}O/\delta^{15}N$ slope of NO_3^- samples consistently has a value of 0.9−1.0,[10−16] whereas terrestrial samples tend to exhibit $\delta^{18}O/\delta^{15}N$ slopes of 0.5−0.7.[17−23] The fact that these slopes are so consistent is consistent with a single origin: that they originate due to a fundamental effect of the NO_3^- oxidation reaction, unaffected by total NO_3^- concentration or size of NO_3^--reducing microbial populations. One hypothesis is that NO_3^- oxidation is controlled by different groups of organisms, consistently using different enzymes, in each environment.[24] An alternative hypothesis is that the natural slope of ∼1 has been overprinted by different signals in the terrestrial environment, including anammox and nitrification, and the presence of enzymatic reversibility,

Received: April 11, 2022
Revised: August 28, 2022
Accepted: September 2, 2022
Published: October 20, 2022

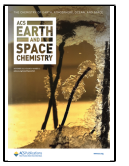

ACS Publications

© 2022 The Authors. Published by American Chemical Society

https://doi.org/10.1021/acsearthspacechem.2c00102
ACS Earth Space Chem. 2022, 6, 2582−2594

forming NO_3^- from NO_2^-.[8,25] The source of the different $^{18}\varepsilon/^{15}\varepsilon$ slopes in different environments, and thus a major control on isotope fractionation in the nitrogen cycle, has yet to be conclusively determined.

Dissimilatory Nitrate Reductases. Both dissimilatory NO_3^- reduction to NH_4^+ and denitrification to N_2 begin with the reduction of NO_3^- to NO_2^-. This initial reduction step is mediated by two classes of dissimilatory NO_3^- reductase enzymes: the periplasmic Nap and the cytosolic Nar. Bacteria are known which express one or both of these enzymes.[26−28] Bacterial cultures containing only Nap have been found to express $^{18}\varepsilon/^{15}\varepsilon$ slopes of 0.43−0.68,[3,24,29,30] whereas most Nar-based NO_3^- reduction imparts a slope of ca. 0.9−1.0.[24,30−32] The similarity in slope dichotomy suggests that environmental differences in $^{18}\varepsilon/^{15}\varepsilon$ may be driven by preferential use of Nar in marine environments and Nap in terrestrial environments. This is possibly due to the use of Nar and not Nap to generate metabolic energy, although NO_3^- respiration is expected to influence N isotope systematics across terrestrial environments.[24] A molecular model of the NapA active site has predicted a $^{18}\varepsilon/^{15}\varepsilon$ slope of 0.6−0.7.[33] In contrast, other molecular models of both NapA and NarG have predicted $^{18}\varepsilon/^{15}\varepsilon$ slopes of 0.9−1.1.[34] Recently, Nar from two *Bacillus* species has been discovered with $^{18}\varepsilon/^{15}\varepsilon$ slopes of 0.61−0.64; their gene sequences form a clade divergent from that of most other Nar reductases.[3]

Nitrate Isotopic Clumping. It has recently become possible to quantify isotopic homologs (isotopologues) of intact NO_3^- and other oxyanions by soft-ionization mass spectrometry (electrospray Orbitrap).[35,36] It is therefore timely to investigate whether rare nitrate isotopologues, such as the doubly substituted nitrate $^{15}N^{18}O^{16}O^{16}O^-$, contain information that can provide novel insights into N cycling processes. "Isotopic clumping" refers to the preferential partitioning of multiple heavy isotopes into the same molecule, most often in a shared bond. The amount of clumping in a compound is defined relative to the hypothetical abundances of the clumped isotopologue in a sample of the same total isotopic composition if all of the isotopes were randomly distributed, i.e., the stochastic distribution. The clumping anomaly $^i\Delta$ for clumped isotopologue i in a sample is conventionally defined as $^i\Delta = (R_{i,\mathrm{sample}}/R_{i,\mathrm{stoch}}) \times 1000‰$, where R_i is the abundance ratio between clumped isotopologue i and the isotopologue with no heavy atom substitutions, i.e., the most common isotopologue. The stochastic abundance ratio $R_{i,\mathrm{stoch}}$ is calculated from the overall abundances of individual isotopes.[37]

Electrospray Orbitrap measurements do not yield $^i\Delta$ directly, but instead ratios between two intact isotopologues, such as $[^{15}N^{18}O^{16}O_2^-]/[^{14}N^{18}O^{16}O_2^-]$ by excluding the dominant peak from the most common isotopologue $^{14}N^{16}O_3^-$.[35,36] Although $^i\Delta$ can be computed by combining two sets of measurements, one with and one without $^{14}N^{16}O_3^-$, the use of two instrument settings can introduce error. Thus, it would be helpful to develop an understanding of the behavior of isotopologues that could be measured without including the dominant $^{14}N^{16}O_3^-$ peak.

Both equilibrium and disequilibrium clumping effects are known. For example, equilibrium clumping between rare heavy isotopes ^{13}C and ^{18}O in carbonate minerals has promoted the extensive growth of carbonate clumped isotope paleothermometry, in which the degree of clumping is sensitive only to temperature and not to overall $\delta^{13}C$ or $\delta^{18}O$ of the minerals or the reactant CO_2 and H_2O from which they formed.[38,39] At equilibrium, clumping is always favored, and $^i\Delta$ is always positive. In contrast, potential disequilibrium clumping signals are known which exhibit both clumping increases[40,41] and decreases[42,43] relative to equilibrium, and some "anticlumping" signals even show selection against clumped isotopes, i.e., negative $^i\Delta$ values. Anticlumping signals can form due to kinetic effects during chemical reactions on either products or residual reactants, diffusion, or statistical effects due to the mixing of different sources.[44−51] Clumping increases are not unambiguously caused by disequilibrium processes, and instead can result from equilibration under nonbulk conditions, such as during catalysis on surfaces.[40] In contrast, anticlumping signals are an unambiguous indicator of disequilibrium, including potentially the mixing of two individually equilibrated sources that have not achieved mutual equilibrium.

In addition to the effects of NO_3^- reduction on N and O isotopes, the step could also have a key influence on $^{15}N-^{18}O$ clumping in NO_3^-. Isotopic clumping in NO_3^- has not yet been explored as an indicator of environmental conditions, and measurements of individual NO_3^- isotopologue abundances including clumped species have only recently been reported.[35,36] Interpretation of $^{15}N-^{18}O$ and $^{18}O-^{18}O$ clumped isotope signals may provide additional information on the process of NO_3^- reduction and uncertainties around the influence of NO_3^- production by nitrification and anammox on ^{15}N and ^{18}O stable isotope dynamics.[25] Clumped isotopes have begun to be investigated in N_2O alongside bulk $\delta^{15}N$ and $\delta^{18}O$, and site preference for ^{15}N,[37,52,53] but we are just beginning to be able to explore clumped isotopes of intact oxyanions.

In this work, we report on molecular models of the NarG active site and make predictions about their intrinsic isotope fractionation based on transition state (TS) theory. We link these intrinsic isotope fractionations to variations in $\delta^{15}N$, $\delta^{18}O$, and $^{15}N-^{18}O$ and $^{18}O-^{18}O$ clumping of residual NO_3^- through the use of a box model representing enzyme reactivity, exploring the co-occurring isotope effects and postulating a use for $^{15}N-^{18}O$ clumping as a proxy record of NO_3^- production and consumption rates.

METHODS

Molecular Modeling. *Rhodobacter sphaeroides* NapA active site models were obtained from a study of N and O isotope effects[33] which adapted the coordinates of the original protein crystallization (PDB: 1OGY).[54] The structures were modified by the replacement of the Cys residue with a monodentate Asp residue to replicate the active site structure of *Escherichia coli* NarG enzyme.[55] To test the effect of cluster cutoff sizes on isotope effects, three different sizes of models were created by cutting the ligands on the catalytic Mo atom in different locations. Cut bonds in all active site models are terminated with H atoms; cuts were made at various points in the molybdopterin guanine dinucleotide cofactors, creating models of different sizes.[33] All models had a single Asp amino acid residue ligating the Mo center, with both peptide bonds cut and replaced with H atoms. NO_3^- was bound to the active site Mo via one O atom. The total electronic charge on all active site models is −2 and the spin multiplicity is 1.

To test the effect of active site hydrophilicity on isotope effects, 0, 3, 6, 9, or 12 H_2O molecules were used to solvate the bound NO_3^- on the smallest active site model, in conjunction with one of two implicit solvation models, or no implicit

https://doi.org/10.1021/acsearthspacechem.2c00102
ACS Earth Space Chem. 2022, 6, 2582−2594

solvation. The implicit solvation models used are the integral-equation-formalism polarizable continuum model (IEFPCM)[56] or the solvation model density (SMD) model.[57] The initial positions of H_2O molecules in our NarG models match those from a previous study of the NapA active site,[33] but these positions adjust during model optimization.

Seventeen molecular models were produced for the NarG active site. Fifteen small active site models (e.g., NarGS) were produced: five levels of explicit solvation by H_2O molecules and three levels of implicit solvation. One medium (NarGM) and one large (NarGL) model were created with no solvation. For each molecular model, both a bound reactant state and a TS were produced.

The molecular modeling software GAUSSIAN 09 revision D.01[58] was used to optimize the coordinates of all molecular models and predict their harmonic frequencies using density functional theory (DFT). For all molecular models, the B3LYP functional[59−61] was used. The basis set LANL2DZ-ECP[62] was used on Mo atoms, and the basis set 6-31+G(d,p)[63−69] was used for all C, H, O, N, and S atoms. Reactants and transition states (TS) were optimized (i.e., energy-minimized) using the Berny algorithm and Tight optimization criteria (maximum/root mean square (RMS) atomic displacement change per step $6 \times 10^{-5}/4 \times 10^{-5}$ b, maximum/RMS force $1.5 \times 10^{-5}/1 \times 10^{-5}$ hartrees/b or hartrees/rad), with an Ultrafine integration grid mesh. Each completed optimization was assessed with a frequency calculation, with no imaginary frequencies for a completed reactant optimization and exactly one imaginary frequency corresponding to the separation of the breaking N−O bond for a completed TS optimization. Frequencies were then recalculated for every possible isotopologue on the NO_3^- ion: ^{14}N and ^{15}N for N; ^{16}O, ^{17}O, and ^{18}O for O, for a total of 54 frequency calculations per molecular model.

In addition to a full set of enzyme-bound NO_3^- and N−O bond-breaking TS models, three models of NO_3^- surrounded by 19 H_2O molecules were created, each with a different continuum solvation treatment. These were optimized to test the ability of the selected computational method to reproduce experimental vibrational spectra of aqueous NO_3^-.

The reduced partition function ratio β was calculated for each isotopologue using the equations

$$^{\text{heavy/light}}\beta_{\text{reac},i} = \prod_i \left(\frac{\nu_{\text{heavy},i}}{\nu_{\text{light},i}} \frac{e^{-h\nu_{\text{heavy},i}/2k_BT}}{1 - e^{-h\nu_{\text{heavy},i}/k_BT}} \frac{1 - e^{-h\nu_{\text{light},i}/k_BT}}{e^{-h\nu_{\text{light},i}/2k_BT}} \right) \quad (1)$$

for reactants, and

$$^{\text{heavy/light}}\beta\text{TS},\ i = \frac{\nu_{\text{heavy}}^{\text{imaginary}}}{\nu_{\text{light}}^{\text{imaginary}}} \times \prod_{\text{no imaginary freq}}^{\text{TS}} \left(\frac{\nu_{\text{heavy},i}}{\nu_{\text{light},i}} \frac{e^{-h\nu_{\text{heavy},i}/2k_BT}}{1 - e^{-h\nu_{\text{heavy},i}/k_BT}} \frac{1 - e^{-h\nu_{\text{light},i}/k_BT}}{e^{-h\nu_{\text{light},i}/2k_BT}} \right) \quad (2)$$

for TS, where ν_i is the vibrational frequency for mode i in s^{-1}, T is the temperature in K, h is Planck's constant, and k_B is the Boltzmann constant. Values of $\nu_{\text{heavy},i}$ are taken from each isotopologue with at least one rare isotope substitution, and values of $\nu_{\text{light},i}$ are taken only from the unsubstituted isotopologue.[70,71] All calculations were made at a temperature of 25 °C. Note that imaginary frequencies only appear in the TS calculation in the leading factor, and not in the product term.[72] Therefore, the reactant β includes $3N - 6$ frequencies in the Π term for models with N atoms, whereas the TS β includes $3N - 7$ frequencies in the Π term.

Reaction Path Modeling. Values of β were integrated into a box model representing NO_3^- binding to the enzyme active site and reduction to NO_2^-. The box models included direct introduction of NO_3^- to the enzyme active site, with the only isotope fractionation resulting from equilibration in the distinguishable O positions of the bound NO_3^-, and irreversible NO_3^- reduction to NO_2^- with associated kinetic isotope fractionation. The box models also consider enzyme concentrations to not be rate-limiting, i.e., reaction kinetics were first-order in NO_3^- only. The box model could be closed, in which case the initial NO_3^- was the only NO_3^- added to the model, or it could be open and steady-state, in which case an additional NO_3^- could be added with isotopologue composition identical to the initial NO_3^- and with total NO_3^- added to balance the amount of NO_2^- formed at all times. The box model could allow isotopomers (isotopologues with the same isotopes but with a different O bound to Mo) to equilibrate, essentially allowing residual NO_3^- to unbind from the enzyme and rebind via a different O, or binding equilibration between isotopomers could be prohibited.

The initial NO_3^- composition was set at equilibrium relative to the abundances of the unsubstituted isotopologue (at an arbitrary abundance of 1.0) and abundances of rare isotopes at approximately natural absolute abundances: ^{15}N at 0.3663%, ^{17}O at 0.0379%, and ^{18}O at 0.20004%.[73] These abundances were used directly for the abundances of the $^{15}N^{16}O_3^-$, $^{14}N^{17}O^{16}O_2^-$, and $^{14}N^{18}O^{16}O_2^-$ isotopologues. All other isotopologues were set at initial isotopic equilibrium based on these abundances: isotopomers j of the singly substituted isotopologues i have their initial abundances set using $K_{eq} = \beta_{\text{reac},j}/\beta_{\text{reac},i}$, and clumped isotopologues have their abundances set using K_{eq} for a reaction involving a single isotope substitution of their first rare isotope. For example, the abundance of $^{15}N^{16}O^{18}O^{16}O$ is set using the reaction

$$^{15}N^{16}O_3^- + {}^{14}N^{16}O^{18}O^{16}O^- \rightleftharpoons {}^{15}N^{16}O^{18}O^{16}O^- + {}^{14}N^{16}O_3^- \quad (3)$$

$$K_{eq} = \frac{\beta_{\text{reac},^{15}N^{16}O^{18}O^{16}O^-}\beta_{\text{reac},^{14}N^{16}O_3^-}}{\beta_{\text{reac},^{15}N^{16}O_3^-}\beta_{\text{reac},^{14}N^{16}O^{18}O^{16}O^-}} = \frac{[^{15}N^{16}O^{18}O^{16}O^-][^{14}N^{16}O_3^-]}{[^{15}N^{16}O_3^-][^{14}N^{16}O^{18}O^{16}O^-]} \quad (4)$$

Note that the position of ^{18}O substitutions is consistent across both sides of eq 3 because the active site breaks the symmetry of the NO_3^- molecule and has different effects on each O. All four β in eq 4, and three of the four concentrations, are known, allowing solution of the doubly clumped concentration. Triply clumped species are then solved using singly and doubly clumped species, and quadruply clumped species are solved using singly and triply clumped species.

https://doi.org/10.1021/acsearthspacechem.2c00102
ACS Earth Space Chem. 2022, 6, 2582−2594

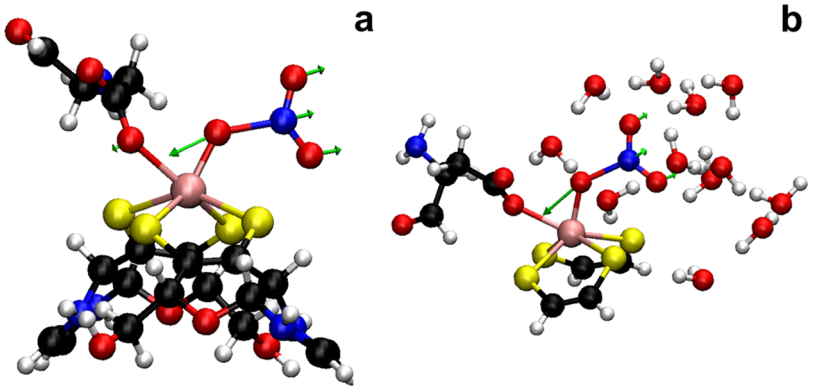

Figure 1. Example TS structures of the NarG active sites. (a) NarGL, 0 H_2O; (b) NarGS, 12 H_2O + PCM. Atoms are colored by element: H (white), C (black), N (blue), O (red), S (yellow), Mo (pink). Green arrows show the motion of the TS imaginary frequency.

Isotopologue-specific first-order rate constants are then calculated as $k_i = k_0(\beta_{TS,i}/\beta_{reac,I})$, where k_0 is the rate constant for the unsubstituted isotopologue. In all model runs, k_0 is set arbitrarily to 1.0. The box model thus produces output using dimensionless concentration and dimensionless time, but the relative concentrations of isotopologues are the important output and are thus unaffected by the nondimensionality.

If isotopomers are allowed to achieve binding equilibrium prior to reaction, a second set of equations is used to accomplish the equilibration without accounting for a separate unbound NO_3^- pool. These equations use a pseudo-rate constant $1000 \times k_0$ in one direction and $1000 \times k_0(\beta_{reac,j}/\beta_{reac,i})$ in the other direction to equilibrate isotopomers i and j, guaranteeing their abundance ratios stay constant and at isotopic equilibrium. For isotopologues with three identical O, no equilibration is necessary. For isotopologues with two identical O, there are three isotopomers to equilibrate. For isotopologues where no O are identical, there are six isotopomers to equilibrate. This step does not equilibrate any nonisotopomers, so no isotope exchange takes place; it only affects binding orientation equilibrium of isotopomers on the active site. Physically, this represents unbinding of NO_3^- isotopologues and rebinding via any of the O atoms, in an equilibrium proportion that is given by $\beta_{reac,j}/\beta_{reac,i}$, e.g., Mo−$^{18}O^{14}N^{16}O^{16}O^-$ can equilibrate with Mo−$^{16}O^{14}N^{18}O^{16}O^-$ and Mo−$^{16}O^{14}N^{16}O^{18}O^-$ without breaking any N−O bonds.

If steady-state conditions are specified instead of closed-system conditions, the total concentration of enzyme-bound NO_3^- is kept constant by ensuring $\sum d[m]/dt = 0$ for all isotopologues m. That is, the total concentration of NO_3^- given by $\sum[m]$ is kept constant by adding NO_3^- with the initial isotopologue composition, given by $[i]_0/\sum[m]_0$ for a given isotopologue i over all isotopologues m, to replace all reacted NO_3^-. This allows the system to approach steady-state concentrations over the course of the box model run.

The differential equation governing the abundance of enzyme-bound NO_3^- isotopologue i as a function of time is thus

$$\frac{d[i]}{dt} = -k_i[i] + \sum_j \left\{ -1000k_0 \frac{\beta_{reac,j}}{\beta_{reac,i}}[i] + 1000k_0[j] \right\} + \left\langle -\left(\sum_m \frac{d[m]}{dt}\right) \times \frac{[i]_0}{\sum_m [m]_0} \right\rangle \quad (5)$$

where the term in curly brackets is included only if isotopomers i and j are allowed to equilibrate, and the term in angle brackets across all isotopologues k is included only if steady-state conditions are specified. The differential equations are solved using the solve_ivp function in Python module SciPy.[74]

Isotope abundances of residual NO_3^- calculated as δ values use the initial composition as a reference state. The calculation for ^{15}R, ^{17}R, and ^{18}R explicitly uses the abundance of each isotope across all isotopologues.

RESULTS

Models and vibrational spectra of aqueous NO_3^- indicate that our selected methods are sufficient to describe molecular vibrations and thus isotope fractionation during NO_3^- reduction (Supporting Information). All NarG molecular models predict N and O kinetic isotope fractionations matching the observed trends in environmental samples (Active Site Model Behavior and Kinetic Isotope Effects (KIEs) sections). Interestingly, the models predict a substantial anticlumping signature in $^{15-18}\Delta$ of NO_3^- during denitrification in a closed system, measurements of which could be used to assess the amount of NO_3^- which has been consumed (Reaction Path Modeling, Closed System section). The anticlumping signature arises primarily because the accumulation of ^{15}N and ^{18}O by Rayleigh fractionation outweighs the accumulation of the clumped isotopologues (Reaction Path Modeling, Closed System with Restricted Binding section). At steady state, the models predict a small clumped $^{15-18}\Delta$ signal along with a larger $^{18-18}\Delta$ signal, measurements of which could be used to assess the influx rate of NO_3^- in a denitrifying system (Reaction Path Modeling, Steady-State System section).

Active Site Model Behavior. We modeled the transition state of the NO_3^- reduction reaction occurring at the NarG active site. We used several related models to ensure our results are not sensitive to the approximations employed in each model. Example TS models are given in Figure 1. Coordinates for all molecular models and 3D animations of example TS models are given in the Supporting Information. Each active site molecular model consists of hexacoordinate Mo, with two bidentate molybdopterin guanine dinucleotide ligands cut depending on model size, one monodentate Asp amino acid ligand, and NO_3^-. The NO_3^- molecular ion binds to Mo via one of its O atoms. In all TS molecular models, the imaginary frequency corresponds to stretching of the N−O bond for this

https://doi.org/10.1021/acsearthspacechem.2c00102
ACS Earth Space Chem. 2022, 6, 2582−2594

O atom; values range from 304.5i to 513.3i cm^{-1}, close to the values of 330i and 476i cm^{-1} reported for two molecular models of NapA.[75] Small amounts of cooperative motion can also be observed in the other ligands and in explicit H_2O molecules. These small cooperative motions do not substantially alter the character of the motion across the TS corresponding to the imaginary frequency. As a result, the TS motion is largely the same across all models.

The ground-state electron configuration of an isolated Mo atom is $[Kr]5s^24d^4$. Prior to NO_3^- reduction, Mo is in the Mo(IV) state and is in the Mo(VI) state after reduction. That makes the likely spin multiplicities of both states singlets: $[Kr]5s^2$ and [Kr], respectively. To verify this, we calculated single-point energies in the singlet and triplet states for NarGL and NarGS with 12 explicit H_2O. The singlet state was the lowest-energy state by 15.1 and 18.8 kcal/mol, respectively. Previous molecular models of similar analogue clusters also found singlets to be the lowest energy state across the potential energy surface of the NO_3^- reduction reaction. In some cases, the difference in energy was small, <1 kcal/mol, albeit accompanied by distortions in the positioning of the cofactors around Mo that are not observed in the X-ray crystallographic structures of NarG. Moreover, experimental results have found no evidence of triplet species in analogue clusters.[76] Therefore, we use singlet multiplicity in all models.

Activation energies including zero-point energies range from 13.0 to 20.2 kcal/mol. Most prior molecular modeling studies have focused on Nap instead of Nar; those studies found activation energies of 11.6 to 19.3 kcal/mol, using a wide range of density functionals and solvation models.[75−78] Only one set of models attempted to model the Nar active site, employing acetate instead of CH_3S^- or $CH_3S_2^-$ as the fifth ligand; it found activation energies of 10.3−17.5 kcal/mol when excluding explicit solvation.[77]

Kinetic Isotope Effects (KIEs). Using the molecular models, we predicted the simultaneous ^{15}N and ^{18}O KIEs, and also the isotope clumping effects, of NarG-catalyzed NO_3^- reduction. The isotope effects are summarized in Table 1. Isotopologue-specific first-order rate constants relative to k_0 are compiled for each model in Table S2 (Supporting Information). The "Best Model" listed comes from the model with 12 explicit H_2O molecules as well as PCM continuum solvation. The same configuration was selected as the "best" model in a study of NapA isotope fractionation.[33]

KIEs are normal for all ^{15}N and ^{18}O isotope substitutions on NO_3^-, including substitutions made on the N−O bonds which are not broken in the TS. Kinetic isotope effects $^{15}\varepsilon$ and $^{18}\varepsilon$ in ‰ can be approximated as $1000(^{15}k/^{14}k - 1)$ or $1000\text{-}(^{18}k_{avg}/^{16}k - 1)$, respectively; the arithmetic averaging for ^{18}O reflects the need to account for isotope effects on the unbroken bonds as well as the breaking one. In the NarG models, $^{15}\varepsilon$ ranges from −36.7 to −31.3‰ and $^{18}\varepsilon$ ranges from −35.5 to −31.6‰. $^{18}O/^{15}N$ isotope slopes for the molecular model are also summarized in Table 1. These values are computed using the output of the reaction path models discussed below, but they can be approximated using $^{18}\varepsilon/^{15}\varepsilon$. All active site $^{18}O/^{15}N$ slopes are ∼1.0. These values are broadly similar to measurements on enzymes,[3] marine cultures,[10,24] and marine environmental samples.[79] Adjusting for possible starting isotope compositions, the molecular model-derived slopes agree well with most of the range of $\delta^{15}N$ and $\delta^{18}O$ from a marine sample database (Figure 2).

Table 1. Kinetic Isotope Parameters Derived from Molecular Models[a]

parameter	minimum	best model	maximum
$^{15}k/^{14}k$	0.9633	0.9637	0.9687
$^{18}k_{avg}/^{16}k$	0.9645	0.9646	0.9684
$^{15-18}k_{avg}/^{14-16}k$	0.9292	0.9296	0.9369
$^{18}\varepsilon/^{15}\varepsilon$ slope	0.942	0.978	1.089
$^{15-18}\Delta$			
0% consumed	0.339	0.352	0.370
80% consumed	−1.756	−1.731	−1.337
90% consumed	−2.667	−2.627	−2.114
$^{15-18}\Delta/^{15}\varepsilon$ slope	−0.037	−0.036	−0.032
$^{18-18}\Delta$			
0% consumed	0.117	0.128	0.137
80% consumed	−0.533	−0.426	0.018
90% consumed	−0.813	−0.664	−0.030
$^{18-18}\Delta/^{15}\varepsilon$ slope	−0.013	−0.009	−0.002

[a]Summarized molecular model-derived kinetic parameters and co-isotope slopes. Individual values are given in the Supporting Information (Table S2). The "Best Model" results come from NarGS $12H_2O$−PCM.

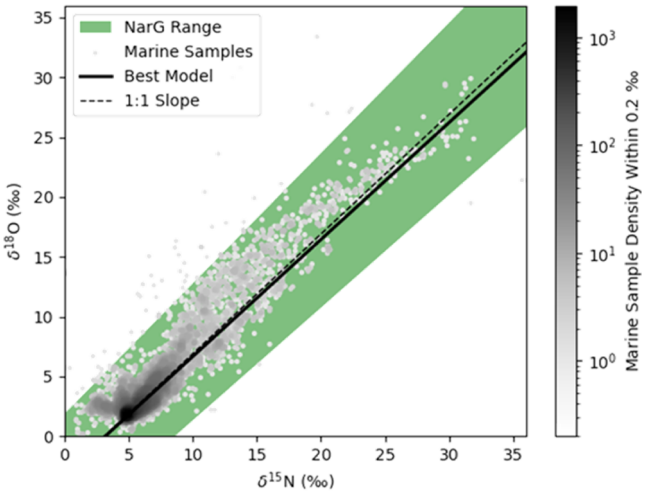

Figure 2. $\delta^{18}O$ vs $\delta^{15}N$ of residual NO_3^-. Solid black curve taken from the NarGS $12H_2O$ + PCM molecular model, fractionating from a closed pool of NO_3^- and overlapping with the high density of marine samples at (5, 2‰); 1:1 slope is shown with same intercept. Ranges of slopes from all models are also shown, including ±5‰ range of intercept values. Points represent a database of marine samples colored by point density.[79]

Emerging developments in electrospray Orbitrap measurements open a route to the use of isotopic clumping in NO_3^- to constrain environmental processes.[35,36] We find that the $^{15}N-^{18}O$ clumping anomaly $^{15-18}\Delta$ in NO_3^- is also influenced by KIEs. Equilibrium $^{15}N-^{18}O$ clumping, as calculated for the active site-bound NO_3^-, is ca. +0.35‰ for all molecular models (Table 1). First-order rate constants for the reaction of each $^{15}N-^{18}O$ clumped isotopologue are also given in Table S2 (Supporting Information). These first-order rate constants are approximately equal to the product of the rate constants of the single isotope substitutions $^{15}k^{18}k$, but are slightly smaller, indicating that the clumped species will react more slowly. This reflects the stabilization of the clumped isotopologue relative to the singly substituted isotopologues. The stabilization is due

https://doi.org/10.1021/acsearthspacechem.2c00102
ACS Earth Space Chem. 2022, 6, 2582−2594

to the lowered zero-point energy of the clumped species. Clumping is favored in the active site-bound NO_3^- (i.e., the value of $^{15-18}\Delta$ is >0) largely because the zero-point energy in the clumped species is lowered more, relative to the unsubstituted species, than the sum of the zero-point energy decreases in the singly substituted species. This effect is typical of all chemical species at equilibrium that can undergo clumping. Clumping is also favored in the TS, but it is favored less than in the reactant, enzyme-bound NO_3^-. This is because the zero-point energy is lowered less in the weakened N−O bonds of the TS than in the reactant. Because the clumped isotopologue in the reactant is stabilized more than the clumped isotopologue is stabilized in the TS, the true clumped reaction rate constant $^{15-18}k < {}^{15}k^{18}k$, and the clumped species reacts more slowly than the singly substituted species and the unsubstituted species. A similar effect on reaction rates is observed during H abstraction from CH_4 by OH or Cl, which can be explained by zero-point energy changes in the reactant and TS.[80] During the course of NO_3^- reduction, clumped NO_3^- will thus concentrate in the residual unreacted fraction. It is tempting to assume that this would lead to an increase in $^{15-18}\Delta$ in the residual NO_3^- pool as the reaction proceeds, in a manner analogous to Rayleigh fractionation on individual isotopes, but this does not occur in a closed system.

Reaction Path Modeling, Closed System. We integrated the kinetic parameters derived from the NarG molecular models into a reaction path model to determine the isotope behavior of NO_3^- during consumption in a closed system. In particular, we modeled the behavior of clumped isotopologues to determine the expected magnitude of clumped isotope effects, and whether Rayleigh-like fractionation controls clumped isotope abundance. The equation for each isotopologue's rate of consumption over time is given by

$$\frac{d[i]}{dt} = -k_i[i] + \sum_j \left\{ -1000k_0 \frac{\beta_{reac,j}}{\beta_{reac,i}}[i] + 1000k_0[j] \right\} \quad (6)$$

for each isotopologue i and for any equivalent isotopomers j, e.g., $^{14}N^{18}O^{16}O_2^-$ and $^{14}N^{16}O^{18}O^{16}O^-$.

In a closed system, the residual NO_3^- left by the NarG model concentrates ^{15}N and ^{18}O, following the expected Rayleigh fractionation pattern (Figure S2) and producing a linear relationship between $\delta^{18}O$ and $\delta^{15}N$ (Figure 2). Slopes for NarG active sites range from 0.942 to 1.089 roughly matching the slopes determined from culture studies of microbes containing NarG.[3] Model size and solvation have no consistent effect on the predicted slopes.

Clumping anomalies $^{15-18}\Delta$ and $^{18-18}\Delta$ are shown in Figure 3. Approximately 65% of all NO_3^- is consumed after one "turnover time", equal to the initial concentration divided by the initial flux, and approximately 87% of all NO_3^- is consumed after two turnover times. Regardless of its initial value, $^{15-18}\Delta$ decreases as NO_3^- is consumed, approximately linearly until ~80% of NO_3^- has been converted to NO_2^-. The net effect on $^{15-18}\Delta$ (final − initial) is −1.90 ± 0.12‰ for NarG at 80% consumption. This occurs despite $^{15-18}k < {}^{15}k^{18}k$; similar behavior has been observed during CH_4 H abstraction by radicals.[80] Anticlumping signals are likely to be generated in residual NO_3^- by reduction via NarG. Depending on variability in the initial NO_3^-, the value of $^{15-18}\Delta$ may be useful as a proxy for the amount of NO_3^- consumed if it can be determined with sufficient precision. In a closed system, the

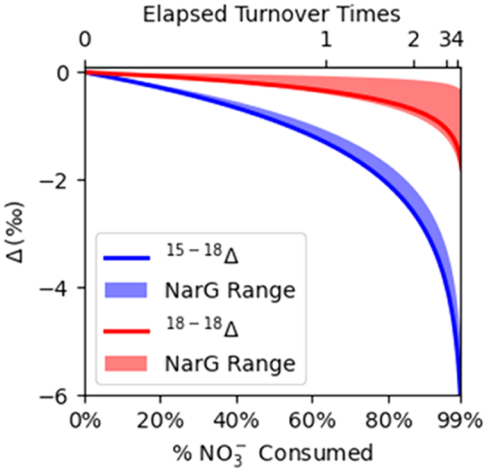

Figure 3. Clumping anomaly $^{15-18}\Delta$ and $^{18-18}\Delta$ of residual NO_3^- in a closed system. Initial composition fixed at $\Delta = 0‰$. Turnover time is calculated as initial amount NO_3^-/initial flux. Curves are taken from the NarGS $12H_2O$ + PCM molecular model. Ranges of values from all molecular models are also shown; individual model parameters are listed in Table S2.

$^{15-18}\Delta/\delta^{15}N$ slope is relatively constant, with some slight curvature at very high (≫90%) consumption (Figure 4).

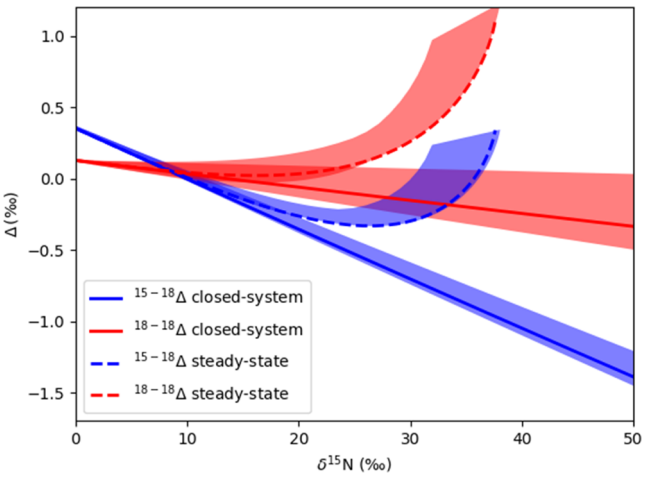

Figure 4. $^{15-18}\Delta$ and $^{18-18}\Delta$ vs $\delta^{15}N$ during closed-system denitrification and approach to steady-state denitrification. Curves are taken from the NarGS $12H_2O$ + PCM molecular model. Ranges of slopes from all models are also shown.

The $^{18}O-{}^{18}O$ clumping anomaly $^{18-18}\Delta$ also decreases and eventually reaches anticlumped values as NO_3^- is consumed. It decreases less severely than $^{15-18}\Delta$ does (Figures 3 and 4), and its precise slope is less well constrained by the molecular models. Determining its value with sufficient precision to use it as a proxy for the proportion NO_3^- consumed would thus likely be more difficult than for $^{15-18}\Delta$. However, $^{18-18}\Delta$ could help constrain whether a denitrifying system is instead operating at, or approaching steady state due to the addition of new NO_3^- (Figure 4; see below).

Reaction Path Modeling, Closed System with Restricted Binding. The purpose of restricting binding is to clarify the source of the anticlumping signal in $^{15-18}\Delta$ generated by NO_3^- reduction (Figure 3). The test may help to discriminate between three hypotheses: (I) The anticlump-

https://doi.org/10.1021/acsearthspacechem.2c00102
ACS Earth Space Chem. 2022, 6, 2582−2594

ing signal is generated by the statistical effect of mixing the two unreacted O atoms on NO_3^- which never bound to Mo with the partially fractionated, residual O atom on the breaking N−O bond.[47,50] (II) The anticlumping signal is generated by preferential reduction of clumped isotopologues, i.e., clumped species react faster than unsubstituted or singly substituted species. (III) The anticlumping signal is generated by preferential reduction of light isotopologues in which increases in the clumped isotopologue's expected stochastic abundance $R_{i,\mathrm{stoch}}$ outpace the actual increase in the clumped isotopologue relative abundance $R_{i,\mathrm{sample}}$. By restricting binding, isotopomers such as $^{15}N^{18}O^{16}O_2^-$ and $^{15}N^{16}O^{18}O^{16}O^-$ can be distinguished. The N−O bonds and thus their clumped values and stochastic isotopologue distributions are rendered distinguishable, and the separate effects of primary isotope effects on the breaking N−O bond, effects on the two other N−O bonds, and statistical effects from mixing their population can be distinguished. The equation for each isotopologue's rate of consumption is given by simple first-order kinetics with no isotopomer equilibration

$$\frac{\mathrm{d}[i]}{\mathrm{d}t} = -k_i[i] \tag{7}$$

Results of the restricted binding model are shown in Figure 5. The increases in $^{15-18}R$ for all three N−O bonds in residual NO_3^- indicate that the abundance of the clumped isotopologue increases relative to the unsubstituted isotopologue in each bond over time. That is, the relative amount of the clumped isotopologue increases as NO_3^- is consumed, invalidating hypothesis II. This matches the prevailing knowledge in a variety of clumped isotope systems, e.g., CH_4 atmospheric sinks, and the theoretical underpinning that zero-point energy is lowered less by clumping in a TS than in a reactant.[80] Although $^{15-18}\Delta$ decreases in the residual NO_3^- pool, this does not indicate clumped NO_3^- reacts faster. Instead, the values of $^{15-18}R_{\mathrm{stoch}}$ increase faster than $^{15-18}R$ increases, resulting in a decrease in $^{15-18}\Delta$ in each bond. Although the reduction of NO_3^- has a normal KIE which causes unsubstituted isotopologues of NO_3^- to react faster, the increase in clumped isotopologues is outweighed by the simultaneous increase in singly substituted isotopologues that make up the definition of the stochastic distribution.

The increase in $^{15-18}R_{\mathrm{N1-O2}}$ can be thought of as a normal primary KIE; the unsubstituted isotopologue reacts faster than the clumped isotopologue. The increases in $^{15-18}R_{\mathrm{N1-O3}}$ and $^{15-18}R_{\mathrm{N1-O4}}$ can likewise be thought of as normal secondary KIEs. Light isotopes react faster even when they are part of the N−O bonds that are not bound to the active site and remain unbroken in product NO_2^-. Large primary and small secondary clumping KIEs have also been identified during CH_4 degradation by radicals.[80] Despite these normal KIEs, the increase in singly substituted isotopologues results in bond-specific $^{15-18}\Delta$ values that decrease for each bond. We point this out to note that decreases in $^{i}\Delta$ in residual reactants do not necessarily indicate inverse KIEs.

The value of $^{15-18}\Delta_{\mathrm{avg}}$ is the arithmetic average of all of the bond-specific $^{15-18}\Delta$ values. It is higher than the true $^{15-18}\Delta_{\mathrm{all}}$ at all times (Figure 5b); the difference between $^{15-18}\Delta_{\mathrm{avg}}$ and $^{15-18}\Delta_{\mathrm{all}}$ represents the impact of hypothesis I above. The reason for the difference is the mixing of N−O bonds of different compositions: two that have not been fractionated by partial N−O bond cleavage, and one that has. The difference in composition of N1−O2 relative to N1−O3 and N1−O4 can

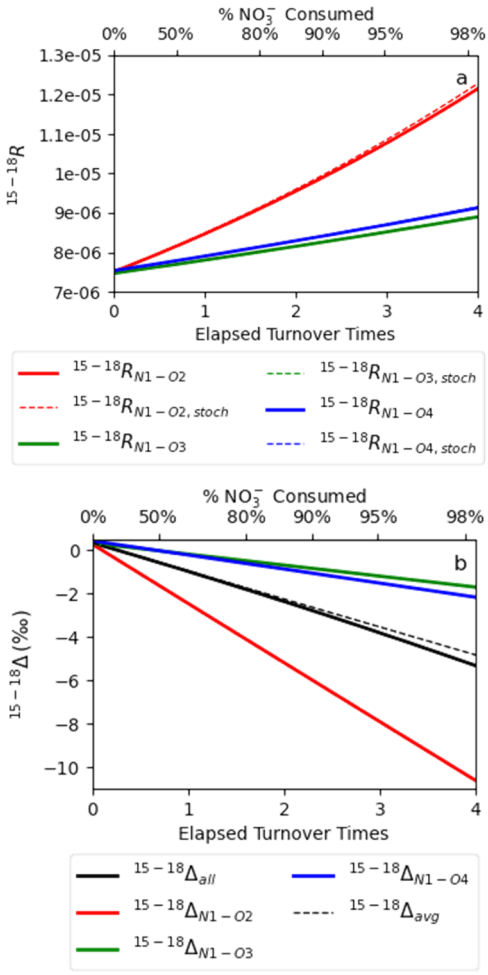

Figure 5. Clumped isotope composition from a closed-system, restricted-binding reaction path model run. Isotope effects are taken from the NarGS $12H_2O$ + PCM molecular model. Clumped isotope composition is shown as (a) $^{15-18}R$ and (b) $^{15-18}\Delta$. Bond-specific values are shown separately for each bond; N1−O2 is the bond that can be catalytically broken at the active site, while N1−O3 and N1−O4 are not bound to the active site and are not cleaved. The value of $^{15-18}\Delta_{\mathrm{avg}}$ reflects the arithmetic average of the bond-specific $^{15-18}\Delta$ values. Turnover time is calculated as the initial amount NO_3^-/initial flux.

be seen in the difference in their $^{15-18}R$ values (Figure 5a), which represents a difference of >10‰ once >98% of the NO_3^- has been consumed. This effect is analogous to the statistical clumped isotope signatures that result from the mixing of atoms of different source compositions.[47,50] The anticlumping signal is partially explained by mixing but is dominated by the increase of stochastic clumped isotopologue abundance relative to the true clumped isotopologue abundance during the NO_3^- reduction reaction with its normal KIEs, i.e., hypothesis III. In other words, most of the anticlumping signal in residual NO_3^- arises because bond-breaking by NarG leaves behind lots of $^{15}N^{16}O_3^-$ and $^{14}N^{18}O^{16}O_2^-$, enough to outweigh the $^{15}N^{18}O^{16}O_2^-$ left behind. A small amount of the anticlumping signal arises because reduction proceeds more slowly for heavy isotopologues even when a bond between the heavy isotopes is not being broken. And a smaller amount still arises from mixing between N−O bonds that were bonded directly to the active site, and N−O bonds that were not.

https://doi.org/10.1021/acsearthspacechem.2c00102
ACS Earth Space Chem. 2022, 6, 2582−2594

As a comparison, we can calculate the maximum clumping effect on $^{15-18}\Delta$, as clumped isotopes do not mix linearly. If marine pools of NO_3^- were mixed with the most extreme values of $\delta^{15}N$ and $\delta^{18}O$ known,[79] with reasonable $^{15-18}\Delta$ values (separated by ≤3‰), then the most nonlinear mixing could affect $^{15-18}\Delta$ is ∼0.35‰ (see the Supporting Information for a calculator). Thus, the $^{15-18}\Delta$ effect of NO_3^- reduction is larger than any expected mixing effect.

Reaction Path Modeling, Steady-State System. In addition to closed systems, steady-state systems are a common endpoint used to understand and interpret isotope behavior. We also modeled steady-state consumption of NO_3^- to consider how the $^i\Delta$ values of a system with constant NO_3^- input might behave. The equation for each isotopologue's rate of consumption is given by

$$\frac{d[i]}{dt} = -k_i[i] + \sum_j \left\{ -1000k_0 \frac{\beta_{reac,j}}{\beta_{reac,i}}[i] + 1000k_0[j] \right\} + -\left(\sum_m \frac{d[m]}{dt}\right) \times \frac{[i]_0}{\sum_m [m]_0} \quad (8)$$

The only difference from the closed-system case is the continuous addition of NO_3^- with the initial isotopologue composition to keep the total concentration of NO_3^- constant.

As expected for an approach to a steady-state system with one input and one output, $\delta^{15}N$ and $\delta^{18}O$ of NO_3^- approach $(1 + \varepsilon)$ because inward flux composition must equal outward flux composition by mass balance (Figure S3a,b). Values of $\delta^{15}N$ and $\delta^{18}O$ approach steady state after approximately 4 turnover times, and $^i\Delta$ values approach steady state after approximately twice this time. The $\delta^{18}O/\delta^{15}N$ slope during the approach to steady state (Figure S3e) is identical to the slope during closed-system consumption of NO_3^- (Figure 2). That is because $\delta^{15}N$ and $\delta^{18}O$ of NO_3^- are controlled by isotopic mass balance, and the approach to steady state is equivalent to mixing between a reacted and unreacted end member. Therefore, the $\delta^{18}O/\delta^{15}N$ slope is unaffected by whether the system is closed to new NO_3^- addition, so long as the input NO_3^- has a constant isotopic composition.

Results for $^{15-18}\Delta$ and $^{18-18}\Delta$ during the approach to steady state are shown in Figure 4 (also see Figure S3c,d for time series). The clumping anomaly $^{15-18}\Delta$ initially decreases as steady state is approached, with a slope equal to that in the closed-system model. However, as steady state is approached, $^{15-18}\Delta$ approximately approaches the value of the input NO_3^-, while $\delta^{15}N$ approaches $(1 + {}^{15}\varepsilon)$, causing the $^{15-18}\Delta/\delta^{15}N$ slope to change dramatically. Because $^{15-18}\Delta$ is not controlled solely by mass balance but also by the arrangement of isotopes, it does not vary in the same way $\delta^{15}N$ does. The $^{15-18}\Delta/\delta^{15}N$ slope could possibly be used as a proxy for the addition of new NO_3^- to the system, even when the new NO_3^- has the same bulk isotopic composition as the original NO_3^-. Steady-state consumption also produces positive values of $^{18-18}\Delta$, which might likewise be used to indicate the new addition of NO_3^- to the system. The larger values of $^{18-18}\Delta$ relative to $^{15-18}\Delta$ can be explained by considering the bonds in each clumped species: two $^{14}N-^{18}O$ and one $^{14}N-^{16}O$ bond, vs one $^{15}N-^{18}O$ and two $^{15}N-^{16}O$ bonds. In contrast to $^{15-18}\Delta$, in which a clumped $^{15}N-^{18}O$ bond can be broken in only one of three possible active site orientations, a heavy $^{14}N-^{18}O$ bond can be broken in two of three possible orientations for $^{18-18}\Delta$. This leads to the slower-reacting $^{18}O-^{18}O$ clumped species accumulating more than $^{15}N-^{18}O$ species. Although $^{15-18}\Delta$ and $^{18-18}\Delta$ change nonmonotonically during the approach to steady state, the individual concentrations of isotopologues do change monotonically (Figure S4). The nonmonotonic behavior of $^{15-18}\Delta$ and $^{18-18}\Delta$ are due to the mixing of an unreacted pool of constant isotopologue compositions with the reacted pool, and the nonlinear changes to Δ values that result from changes to the stochastic distribution with changing bulk isotopic composition. Similar nonmonotonic evolution of $^i\Delta$ is observed in models of DIC isotope exchange and CO_2 absorption/degassing.[46]

DISCUSSION

In this study, we make the first reported predictions for isotopic clumping in residual NO_3^- left behind by NarG and make the first proposed uses for $^{15-18}\Delta$ and $^{18-18}\Delta$ for a proxy record of N cycling. Experimental evaluation of clumping produced in residual NO_3^- could help further solve the puzzle of differences in the isotope effects of NarG and help to tie those effects more directly to observations of N and O isotope fractionation observed in the environment during NO_3^- reduction. Furthermore, the measurement of isotopic clumping could give additional information on the details of environmental nitrogen cycling processes, including reaction mechanisms, reversibility, and system closure and fluxes.

O/N Slope Prediction. Considering fractionation imparted solely by the N−O bond-breaking step at the active site, NarG is predicted to produce $\delta^{18}O/\delta^{15}N$ slopes of 1.0 ± 0.1. The TS imaginary modes corresponding to the breaking of the N−O bond are similar across all models, explaining why there is little variability in slope. Thus, bond-breaking at the active site can explain most of the isotope trend produced by NarG (Figure 2). Overall, this modeling study suggests that the NarG molecular models reproduce the observed slope of ∼1.0 because NarG is well represented by a reversibly binding, irreversibly reacting single-step reaction to break the N−O bond. The NapA enzyme likely either has partially irreversible NO_3^- binding, partially reversible NO_2^- reoxidation prior to H_2O release or active site reduction, or a combination of the two.

Isotopic Clumping in NO_3^- and Link to Empirical Observations. Clumping measurements in NO_3^- are now becoming feasible.[35,36] Such measurements could help track many processes in the nitrogen cycle. The advent of these analytical capabilities motivates the need for theoretical predictions of isotopic clumping in response to different nitrogen cycle processes. This study provides a starting point to consider the abundances of clumped isotopologues of intact populations of NO_3^-. It also suggests three possible uses for measurements of $^{15-18}\Delta$. First, the anticlumping signal expected as a result of NO_3^- reduction could be used to reconstruct the amount of NO_3^- consumed and the original concentration of NO_3^- in a closed system. Second, the constant $^{15-18}\Delta/\delta^{15}N$ slope in closed systems could be used to reconstruct the original $\delta^{15}N$ of NO_3^-. Third, the difference in $^{15-18}\Delta/\delta^{15}N$ slope behavior between closed systems and systems approaching steady state could be used to assess the degree to which new NO_3^- is being added to a system undergoing NO_3^- reduction.

In a closed system, $^{15-18}\Delta$ is predicted to decrease roughly linearly in response to the amount of NO_3^- that has been consumed. This linear trend continues to ∼80% NO_3^- consumption, at which point continued NO_3^- reduction

https://doi.org/10.1021/acsearthspacechem.2c00102
ACS Earth Space Chem. 2022, 6, 2582−2594

results in a dramatic decrease in $^{15-18}\Delta$. At first glance, this behavior appears similar to Rayleigh fractionation, in which continued consumption of clumped NO_3^- produced residual NO_3^- with more and more negative $^{15-18}\Delta$ values. However, this is not truly Rayleigh fractionation, for two reasons. First, Rayleigh fractionation occurs because of mass balance, where e.g., one heavy isotope is preferentially depleted in residual reactants as isotopically heavy products are continuously removed from the system. Because individual isotopes are not created nor destroyed, mass balance dictates that enrichment in products causes depletion in reactants, or vice versa. However, clumped isotopologues can be created or destroyed, as they represent only an arrangement of the available isotopes. Mass balance expressions can track reactions of individual isotopologues if bonds are not formed or broken, or if newly formed or broken bonds are tracked. However, it would be impossible experimentally to track e.g., $^{15}N^{16}O_2^-$ formed by cleavage of a $^{15}N-^{16}O$ bond in NO_3^- separately from $^{15}N^{16}O_2^-$ formed by cleavage of a $^{15}N-^{18}O$ bond. A second reason that this behavior is not true Rayleigh fractionation is that the proportion of clumped isotopologues relative to the unsubstituted isotopologue actually increases as NO_3^- is consumed (Figure 5a). Despite the accumulation of clumped isotopologues, the $^{15-18}\Delta$ value decreases because the value of $^{15-18}\Delta$ is dependent on the overall isotopic composition of the residual NO_3^- and thus is dependent on the singly substituted isotopologue abundances $[^{15}N^{16}O_3^-]$ and $\sum[^{14}N^{18}O^{16}O_2^-]$ as well as the unsubstituted isotopologue abundance $[^{14}N^{16}O_3^-]$. The dependence of $^i\Delta$ on bulk isotopic composition through modifications of the stochastic abundance reference has been discussed previously in other systems.[81,82]

For processes with co-occurring isotope fractionations and clumping effects, it is possible to conserve $^i\Delta$ values only if there are particular mathematical relationships between fractionation factors.[82,83] Those relationships often rely on there being a consistent, mass-dependent relationship between isotopes of the same element, e.g., ^{18}O and ^{17}O. However, there is no general mass-dependent relationship between fractionations of different elements, e.g., $^{15}N/^{14}N$ and $^{18}O/^{16}O$ that holds in all bond-breaking processes. For processes that involve either steady-state or closed-system fractionation within a system with one sink and at most one source, Whitehill et al.[80] have derived expressions that can describe variations in $^i\Delta$ as a function of individual isotope effects and can thus be used to derive what the values of isotope clumping effects would need to be to conserve $^{15-18}\Delta$ values in this system. For a steady-state system, $^{15-18}k = {}^{15}k{}^{18}k$ will conserve the original $^{15-18}\Delta$ value. For a closed system, using the range of rate constant values in Table 1, $^{15-18}k/{}^{15}k{}^{18}k$ = 0.99860−0.99901 would conserve $^{15-18}\Delta$ values. For smaller values of $^{15-18}k/{}^{15}k{}^{18}k$, $^{15-18}\Delta$ would increase in residual NO_3^- during closed-system fractionation, and for larger values, $^{15-18}\Delta$ would increase (as we observe across all models). The $^{15-18}\Delta$-conserving value implies that $^{15}N^{18}O^{16}O_2^-$ would have to be 0.99−1.40‰ less abundant in the TS than in the reactant. Because reactant NO_3^- has a $^{15-18}\Delta$ of 0.34−0.37‰, conserving $^{15-18}\Delta$ would require that $^{15}N^{18}O^{16}O_2^-$ be less stable in the TS than $^{14}N^{16}O_3^-$. This is not expected to be possible, as zero-point energy stabilization should favor clumping in any molecular species including a TS, albeit less than in stable reactants. Therefore, we expect the $^{15-18}\Delta$ decline in closed systems to be robust.

The existence of anticlumping signals generated by statistical effects due to the mixing of different pools of atoms has been described.[47,50] The anticlumping signal expected in residual NO_3^- can be partially a result of those statistical effects (Figure 5b), where the pools are unreacted and partially broken N−O bonds. However, the anticlumping signal is dominated by simultaneous increases in the proportion of ^{15}N, ^{18}O, and $^{15}N-^{18}O$ clumped isotopologues in the residual NO_3^-. This occurs even though the clumped NO_3^- isotopologues react more slowly than either the singly substituted or unsubstituted isotopologues. So long as the energetic benefit of clumping is small relative to the energetic benefit of single isotope substitutions, anticlumping signals can be generated in the residual reactant of a kinetically controlled reaction, due to the stochastic abundance of clumped isotopologues exceeding the true abundance. Even in reactions in which clumping's energetic favorability is identical in reactant and TS, anticlumping signals will result from closed-system fractionation due to the prevalence of normal KIEs for single isotope substitutions.[80] Similar effects have been observed in both bond-breaking and bond-conserving processes, including gas diffusion,[44,82,84] release of CO_2 by carbonates,[85,86] ethane cracking[87] and methane production[88,89] and consumption,[80] where the accumulation of light isotopes is associated with increases in $^i\Delta$ (or accumulation of heavy isotopes is associated with decreases in $^i\Delta$) because of the convention of referencing to the stochastic abundance when measuring clumped isotopologues.

The constant $^{15-18}\Delta/\delta^{15}N$ slope in closed-system models suggests that the slope could be used to reconstruct the original $\delta^{15}N$ of NO_3^-. This would require substantial accuracy of $^{15-18}\Delta$ measurement, as the slopes are predicted to be fairly flat, ca. −0.035‰ clumping/1‰ $\delta^{15}N$ (Table 1). A ∼30‰ change in $\delta^{15}N$ would thus be associated with only a 1‰ depletion in $^{15-18}\Delta$. Moreover, the initial $^{15-18}\Delta$ value would need to be somehow constrained to make the reconstruction. If the original NO_3^- is at internal clumping equilibrium, this could be possible, although it is likely that any NO_3^- formed during nitrification would not be at internal isotopic equilibrium. It would also be possible to make the reconstruction if NO_3^- formed during nitrification has a constant $^{15-18}\Delta$. The value of $^{15-18}\Delta$ produced by nitrification has not yet been experimentally constrained.

Because $^{15-18}\Delta$ behaves differently in a system approaching steady state (Figure 4), $^{15-18}\Delta/\delta^{15}N$ slope could be useful to indicate systems in which NO_3^- is being continuously added vs those where NO_3^- addition has ceased. Much like the reason that the closed-system anticlumping signal is not true Rayleigh fractionation, the change in slope in approach to steady-state conditions is caused by the lack of mass balance control on Δ values. If NO_3^- samples are found which do not have consistent variation between $^{15-18}\Delta$ and $\delta^{15}N$, or if the slope is found to differ substantially from −0.035, that could indicate additional ongoing sources of NO_3^-. Determining the input rate of those sources, or their isotopic composition, would likely require fitting of a reaction path model similar to that described in this study, with terms for both sources and sinks whose compositions could vary over time or in response to certain perturbations. For simple cases where a single source of NO_3^- does have nearly constant isotopologue composition and steady state is achieved, the final values of $^{15-18}\Delta$ and $^{18-18}\Delta$ should be offset from the $^{15-18}\Delta$ and $^{18-18}\Delta$ values of the input NO_3^- by constant offsets[80] equal to the difference in initial and

https://doi.org/10.1021/acsearthspacechem.2c00102
ACS Earth Space Chem. 2022, 6, 2582−2594

final compositions shown in the steady-state cases in Figure 4 and governed by the reaction KIEs. That is, the change in $^{i}\Delta$ upon reaching steady state, relative to the input $^{i}\Delta$, should be insensitive to initial composition, at least near natural isotope abundances. The shape of the nonmonotonic evolution in $^{i}\Delta$ is explained and supported by a derivation given in the Supporting Information. Similar nonmonotonic behavior is predicted during the evolution of dissolved inorganic carbon clumped isotope compositions in processes such as isotope exchange with H_2O and degassing.[46]

NapA is known to produce an $^{18}\varepsilon/^{15}\varepsilon$ slope of 0.5−0.6, much different from that of NarG. Its clumped isotope effects are thus also likely to differ from those of NarG. Future work will be needed to constrain the clumped isotope effects of NapA, and potentially reveal the proportion of denitrification proceeding via NapA vs NarG by the measurement of clumped isotopologues.

The behavior of $^{18-18}\Delta$ is predicted to complement that of $^{15-18}\Delta$. Like $^{15-18}\Delta$, $^{18-18}\Delta$ decreases in Rayleigh-like closed-system fractionation to potentially anticlumping values, despite an accumulation of clumped species relative to the most common isotopologue. However, the decrease in $^{18-18}\Delta$ is much more gradual and may not reach anticlumped values even at relatively high $\delta^{15}N$ values (Figure 4). Also, the $^{18-18}\Delta$ value is predicted to be higher than the value of $^{15-18}\Delta$ at steady state. The steady-state $^{18}O-^{18}O$ clumping is predicted to be substantial despite the absence of a shared bond between them. Potentially, measurements of $^{18-18}\Delta$ could be compared to $^{15-18}\Delta$ to help constrain production vs consumption rates.

Electrospray Orbitrap measurements record ratios between two isotopologues, and do not reveal $^{i}\Delta$ values directly. The values can be computed in a straightforward way, without the need for a stochastic reference material, but computation requires measurement both with and without the dominant $^{14}N^{16}O_3^-$ peak, compounding error from two measurement settings. We report $^{15-18}\Delta$ and $^{18-18}\Delta$ here as it matches the convention of clumped measurements made on other geochemical species, and because we are still developing the best way to measure intact clumped isotope abundances with the least error on electrospray Orbitrap instruments. It is possible that reporting isotopologue abundance ratios directly such as $[^{15}N^{18}O]/[^{15}N]$ or $[^{18}O^{18}O]/[^{18}O]$, or more unconventional Orbitrap ratios such as $[^{15}N^{18}O]/[^{18}O^{18}O]$,[35] might be a solution. Developments in this regard will require more studies such as this one which consider the way in which multiple clumped isotopologues behave simultaneously during chemical reactions. Such insights may also extend to other intact ion populations, such as the many clumped isotopologues of SO_4^{2-}.

■ ASSOCIATED CONTENT

Supporting Information

The Supporting Information is available free of charge at https://pubs.acs.org/doi/10.1021/acsearthspacechem.2c00102.

Molecular model *XYZ* coordinates, TS animations, NO_3^- (aq) modeled vibrational frequencies vs experiment, kinetic isotope parameters from individual molecular models, graphs of closed-system ^{15}N and ^{18}O Rayleigh fractionation, graphs of isotopic composition during approach to steady state, and a spreadsheet-based clumped isotopologue mixing calculator (PDF)

Mixing calculator (XLSX)

■ AUTHOR INFORMATION

Corresponding Author

Jason D. Boettger − *Department of Earth, Environmental, and Resource Sciences, The University of Texas at El Paso, El Paso, Texas 79968, United States;* orcid.org/0000-0002-2853-8772; Email: jdboettger@utep.edu

Authors

Cajetan Neubauer − *Department of Geological Sciences & Institute of Arctic and Alpine Research, University of Colorado, Boulder, Colorado 80303, United States;* orcid.org/0000-0002-5348-5609

Sebastian H. Kopf − *Department of Geological Sciences & Institute of Arctic and Alpine Research, University of Colorado, Boulder, Colorado 80303, United States*

James D. Kubicki − *Department of Earth, Environmental, and Resource Sciences, The University of Texas at El Paso, El Paso, Texas 79968, United States;* orcid.org/0000-0002-9277-9044

Complete contact information is available at: https://pubs.acs.org/10.1021/acsearthspacechem.2c00102

Notes

The authors declare no competing financial interest.

■ ACKNOWLEDGMENTS

Computations were performed using the Advanced CyberInfrastructure computational resources provided by the Penn State Institute for CyberScience. This material is also based upon research supported by the National Aeronautics and Space Administration through the NASA Astrobiology Institute under Cooperative Agreement no. 80NSSC18M0094 issued through the Science Mission Directorate; this grant supported the work of J.D.B. C.N. and S.H.K. were supported by National Science Foundation award #2041539. The authors gratefully acknowledge the helpful review of L. Yeung, which has served to improve the manuscript.

■ REFERENCES

(1) Kuypers, M. M. M.; Marchant, H. K.; Kartal, B. The Microbial Nitrogen-Cycling Network. *Nat. Rev. Microbiol.* **2018**, *16*, 263−276.

(2) Gruber, N.; Galloway, J. N. An Earth-System Perspective of the Global Nitrogen Cycle. *Nature* **2008**, *451*, 293−296.

(3) Asamoto, C. K.; Rempfert, K. R.; Luu, V. H.; Younkin, A. D.; Kopf, S. H. Enzyme-Specific Coupling of Oxygen and Nitrogen Isotope Fractionation of the Nap and Nar Nitrate Reductases. *Environ. Sci. Technol.* **2021**, *55*, 5537−5546.

(4) Brunner, B.; Contreras, S.; Lehmann, M. F.; Matantseva, O.; Rollog, M.; Kalvelage, T.; Klockgether, G.; Lavik, G.; Jetten, M. S. M.; Kartal, B.; Kuypers, M. M. M. Nitrogen Isotope Effects Induced by Anammox Bacteria. *Proc. Natl. Acad. Sci. U.S.A.* **2013**, *110*, 18994−18999.

(5) Buchwald, C.; Casciotti, K. L. Oxygen Isotopic Fractionation and Exchange during Bacterial Nitrite Oxidation. *Limnol. Oceanogr.* **2010**, *55*, 1064−1074.

(6) Carpenter, E. J.; Harvey, H. R.; Fry, B.; Capone, D. G. Biogeochemical Tracers of the Marine Cyanobacterium Trichodesmium. *Deep Sea Res., Part I* **1997**, *44*, 27−38.

(7) Denk, T. R. A.; Mohn, J.; Decock, C.; Lewicka-Szczebak, D.; Harris, E.; Butterbach-Bahl, K.; Kiese, R.; Wolf, B. The Nitrogen

Cycle: A Review of Isotope Effects and Isotope Modeling Approaches. *Soil Biol. Biochem.* **2017**, *105*, 121−137.
(8) Kobayashi, K.; Makabe, A.; Yano, M.; Oshiki, M.; Kindaichi, T.; Casciotti, K. L.; Okabe, S. Dual Nitrogen and Oxygen Isotope Fractionation during Anaerobic Ammonium Oxidation by Anammox Bacteria. *ISME J.* **2019**, *13*, 2426−2436.
(9) Magyar, P. M.; Hausherr, D.; Niederdorfer, R.; Stöcklin, N.; Wei, J.; Mohn, J.; Bürgmann, H.; Joss, A.; Lehmann, M. F. Nitrogen Isotope Effects Can Be Used to Diagnose N Transformations in Wastewater Anammox Systems. *Sci. Rep.* **2021**, *11*, No. 7850.
(10) Granger, J.; Sigman, D. M.; Needoba, J. A.; Harrison, P. J. Coupled Nitrogen and Oxygen Isotope Fractionation of Nitrate during Assimilation by Cultures of Marine Phytoplankton. *Limnol. Oceanogr.* **2004**, *49*, 1763−1773.
(11) Casciotti, K. L.; McIlvin, M. R. Isotopic Analyses of Nitrate and Nitrite from Reference Mixtures and Application to Eastern Tropical North Pacific Waters. *Mar. Chem.* **2007**, *107*, 184−201.
(12) DiFiore, P. J.; Sigman, D. M.; Dunbar, R. B. Upper Ocean Nitrogen Fluxes in the Polar Antarctic Zone: Constraints from the Nitrogen and Oxygen Isotopes of Nitrate: Polar Antarctic Nitrate N and O Isotopes. *Geochem. Geophys. Geosyst.* **2009**, *10*, No. Q11016.
(13) Casciotti, K. L.; Buchwald, C.; McIlvin, M. Implications of Nitrate and Nitrite Isotopic Measurements for the Mechanisms of Nitrogen Cycling in the Peru Oxygen Deficient Zone. *Deep Sea Res., Part I* **2013**, *80*, 78−93.
(14) Gaye, B.; Nagel, B.; Dähnke, K.; Rixen, T.; Emeis, K.-C. Evidence of Parallel Denitrification and Nitrite Oxidation in the ODZ of the Arabian Sea from Paired Stable Isotopes of Nitrate and Nitrite: Arabian Sea Nitrogen Cycling. *Global Biogeochem. Cycles* **2013**, *27*, 1059−1071.
(15) Rafter, P. A.; DiFiore, P. J.; Sigman, D. M. Coupled Nitrate Nitrogen and Oxygen Isotopes and Organic Matter Remineralization in the Southern and Pacific Oceans: Nitrate Isotopes and Remineralization. *J. Geophys. Res.: Oceans* **2013**, *118*, 4781−4794.
(16) Bourbonnais, A.; Letscher, R. T.; Bange, H. W.; Échevin, V.; Larkum, J.; Mohn, J.; Yoshida, N.; Altabet, M. A. N_2O Production and Consumption from Stable Isotopic and Concentration Data in the Peruvian Coastal Upwelling System: N_2O Production and Consumption off Peru. *Global Biogeochem. Cycles* **2017**, *31*, 678−698.
(17) Aravena, R.; Robertson, W. D. Use of Multiple Isotope Tracers to Evaluate Denitrification in Ground Water: Study of Nitrate from a Large-Flux Septic System Plume. *Ground Water* **1998**, *36*, 975−982.
(18) Böttcher, J.; Strebel, O.; Voerkelius, S.; Schmidt, H.-L. Using Isotope Fractionation of Nitrate-Nitrogen and Nitrate-Oxygen for Evaluation of Microbial Denitrification in a Sandy Aquifer. *J. Hydrol.* **1990**, *114*, 413−424.
(19) Cey, E. E.; Rudolph, D. L.; Aravena, R.; Parkin, G. Role of the Riparian Zone in Controlling the Distribution and Fate of Agricultural Nitrogen near a Small Stream in Southern Ontario. *J. Contam. Hydrol.* **1999**, *37*, 45−67.
(20) Houlton, B. Z.; Sigman, D. M.; Hedin, L. O. Isotopic Evidence for Large Gaseous Nitrogen Losses from Tropical Rainforests. *Proc. Natl. Acad. Sci. U.S.A.* **2006**, *103*, 8745−8750.
(21) Lehmann, M. F.; Reichert, P.; Bernasconi, S. M.; Barbieri, A.; McKenzie, J. A. Modelling Nitrogen and Oxygen Isotope Fractionation during Denitrification in a Lacustrine Redox-Transition Zone. *Geochim. Cosmochim. Acta* **2003**, *67*, 2529−2542.
(22) Mengis, M.; Schif, S. L.; Harris, M.; English, M. C.; Aravena, R.; Elgood, R.; MacLean, A. Multiple Geochemical and Isotopic Approaches for Assessing Ground Water NO_3^- Elimination in a Riparian Zone. *Ground Water* **1999**, *37*, 448−457.
(23) Wenk, C. B.; Zopfi, J.; Blees, J.; Veronesi, M.; Niemann, H.; Lehmann, M. F. Community N and O Isotope Fractionation by Sulfide-Dependent Denitrification and Anammox in a Stratified Lacustrine Water Column. *Geochim. Cosmochim. Acta* **2014**, *125*, 551−563.
(24) Granger, J.; Sigman, D. M.; Lehmann, M. F.; Tortell, P. D. Nitrogen and Oxygen Isotope Fractionation during Dissimilatory Nitrate Reduction by Denitrifying Bacteria. *Limnol. Oceanogr.* **2008**, *53*, 2533−2545.
(25) Granger, J.; Wankel, S. D. Isotopic Overprinting of Nitrification on Denitrification as a Ubiquitous and Unifying Feature of Environmental Nitrogen Cycling. *Proc. Natl. Acad. Sci. U.S.A.* **2016**, *113*, E6391−E6400.
(26) González, P.; Correia, C.; Moura, I.; Brondino, C. D.; Moura, J. J. G. Bacterial Nitrate Reductases: Molecular and Biological Aspects of Nitrate Reduction. *J. Inorg. Biochem.* **2006**, *100*, 1015−1023.
(27) Philippot, L. Denitrifying Genes in Bacterial and Archaeal Genomes. *Biochim. Biophys. Acta, Gene Struct. Expression* **2002**, *1577*, 355−376.
(28) Richardson, D. J.; Berks, B. C.; Russell, D. A.; Spiro, S.; Taylor, C. J. Functional, Biochemical and Genetic Diversity of Prokaryotic Nitrate Reductases. *Cell. Mol. Life Sci.* **2001**, *58*, 165−178.
(29) Frey, C.; Hietanen, S.; Jürgens, K.; Labrenz, M.; Voss, M. N and O Isotope Fractionation in Nitrate during Chemolithoautotrophic Denitrification by *Sulfurimonas gotlandica*. *Environ. Sci. Technol.* **2014**, *48*, 13229−13237.
(30) Treibergs, L. A.; Granger, J. Enzyme Level N and O Isotope Effects of Assimilatory and Dissimilatory Nitrate Reduction. *Limnol. Oceanogr.* **2017**, *62*, 272−288.
(31) Kritee, K.; Sigman, D. M.; Granger, J.; Ward, B. B.; Jayakumar, A.; Deutsch, C. Reduced Isotope Fractionation by Denitrification under Conditions Relevant to the Ocean. *Geochim. Cosmochim. Acta* **2012**, *92*, 243−259.
(32) Wunderlich, A.; Meckenstock, R.; Einsiedl, F. Effect of Different Carbon Substrates on Nitrate Stable Isotope Fractionation During Microbial Denitrification. *Environ. Sci. Technol.* **2012**, *46*, 4861−4868.
(33) He, Y.; Zhang, Y.; Zhang, S.; Liu, Y. Predicting Nitrogen and Oxygen Kinetic Isotope Effects of Nitrate Reduction by Periplasmic Dissimilatory Nitrate Reductase. *Geochim. Cosmochim. Acta* **2021**, *293*, 224−239.
(34) Guo, W.; Granger, J.; Sigman, D. M. In *Nitrate Isotope Fractionations during Biological Nitrate Reduction: Insights from First Principles Theoretical Modeling*; American Geophysical Union, 2010; pp PP34A-08.
(35) Hilkert, A.; Böhlke, J. K.; Mroczkowski, S. J.; Fort, K. L.; Aizikov, K.; Wang, X. T.; Kopf, S. H.; Neubauer, C. Exploring the Potential of Electrospray-Orbitrap for Stable Isotope Analysis Using Nitrate as a Model. *Anal. Chem.* **2021**, *93*, 9139−9148.
(36) Neubauer, C.; Crémière, A.; Wang, X. T.; Thiagarajan, N.; Sessions, A. L.; Adkins, J. F.; Dalleska, N. F.; Turchyn, A. V.; Clegg, J. A.; Moradian, A.; Sweredoski, M. J.; Garbis, S. D.; Eiler, J. M. Stable Isotope Analysis of Intact Oxyanions Using Electrospray Quadrupole-Orbitrap Mass Spectrometry. *Anal. Chem.* **2020**, *92*, 3077−3085.
(37) Wang, Z.; Schauble, E. A.; Eiler, J. M. Equilibrium Thermodynamics of Multiply Substituted Isotopologues of Molecular Gases. *Geochim. Cosmochim. Acta* **2004**, *68*, 4779−4797.
(38) Eiler, J. M. Paleoclimate Reconstruction Using Carbonate Clumped Isotope Thermometry. *Quat. Sci. Rev.* **2011**, *30*, 3575−3588.
(39) Ghosh, P.; Adkins, J.; Affek, H.; Balta, B.; Guo, W.; Schauble, E. A.; Schrag, D.; Eiler, J. M. 13C−18O Bonds in Carbonate Minerals: A New Kind of Paleothermometer. *Geochim. Cosmochim. Acta* **2006**, *70*, 1439−1456.
(40) Yeung, L. Y.; Affek, H. P.; Hoag, K. J.; Guo, W.; Wiegel, A. A.; Atlas, E. L.; Schauffler, S. M.; Okumura, M.; Boering, K. A.; Eiler, J. M. Large and Unexpected Enrichment in Stratospheric $^{16}O^{13}C^{18}O$ and Its Meridional Variation. *Proc. Natl. Acad. Sci. U.S.A.* **2009**, *106*, 11496−11501.
(41) Saenger, C.; Affek, H. P.; Felis, T.; Thiagarajan, N.; Lough, J. M.; Holcomb, M. Carbonate Clumped Isotope Variability in Shallow Water Corals: Temperature Dependence and Growth-Related Vital Effects. *Geochim. Cosmochim. Acta* **2012**, *99*, 224−242.
(42) Kluge, T.; Affek, H. P. Quantifying Kinetic Fractionation in Bunker Cave Speleothems Using Δ47. *Quat. Sci. Rev.* **2012**, *49*, 82−94.

https://doi.org/10.1021/acsearthspacechem.2c00102
ACS Earth Space Chem. 2022, 6, 2582−2594

(43) Loyd, S. J.; Sample, J.; Tripati, R. E.; Defliese, W. F.; Brooks, K.; Hovland, M.; Torres, M.; Marlow, J.; Hancock, L. G.; Martin, R.; Lyons, T.; Tripati, A. E. Methane Seep Carbonates Yield Clumped Isotope Signatures out of Equilibrium with Formation Temperatures. *Nat. Commun.* **2016**, *7*, No. 12274.
(44) Eiler, J. M. The Isotopic Anatomies of Molecules and Minerals. *Annu. Rev. Earth Planet. Sci.* **2013**, *41*, 411−441.
(45) Eiler, J. M.; Bergquist, B.; Bourg, I.; Cartigny, P.; Farquhar, J.; Gagnon, A.; Guo, W.; Halevy, I.; Hofmann, A.; Larson, T. E.; Levin, N.; Schauble, E. A.; Stolper, D. Frontiers of Stable Isotope Geoscience. *Chem. Geol.* **2014**, *372*, 119−143.
(46) Guo, W. Kinetic Clumped Isotope Fractionation in the DIC-H2O-CO2 System: Patterns, Controls, and Implications. *Geochim. Cosmochim. Acta* **2020**, *268*, 230−257.
(47) Röckmann, T.; Popa, M. E.; Krol, M. C.; Hofmann, M. E. G. Statistical Clumped Isotope Signatures. *Sci. Rep.* **2016**, *6*, No. 31947.
(48) Stolper, D. A.; Martini, A. M.; Clog, M.; Douglas, P. M.; Shusta, S. S.; Valentine, D. L.; Sessions, A. L.; Eiler, J. M. Distinguishing and Understanding Thermogenic and Biogenic Sources of Methane Using Multiply Substituted Isotopologues. *Geochim. Cosmochim. Acta* **2015**, *161*, 219−247.
(49) Wang, D. T.; Gruen, D. S.; Lollar, B. S.; Hinrichs, K.-U.; Stewart, L. C.; Holden, J. F.; Hristov, A. N.; Pohlman, J. W.; Morrill, P. L.; Konneke, M.; Delwiche, K. B.; Reeves, E. P.; Sutcliffe, C. N.; Ritter, D. J.; Seewald, J. S.; McIntosh, J. C.; Hemond, H. F.; Kubo, M. D.; Cardace, D.; Hoehler, T. M.; Ono, S. Nonequilibrium Clumped Isotope Signals in Microbial Methane. *Science* **2015**, *348*, 428−431.
(50) Yeung, L. Y. Combinatorial Effects on Clumped Isotopes and Their Significance in Biogeochemistry. *Geochim. Cosmochim. Acta* **2016**, *172*, 22−38.
(51) Yeung, L. Y.; Ash, J. L.; Young, E. D. Biological Signatures in Clumped Isotopes of O2. *Science* **2015**, *348*, 431−434.
(52) Schmidt, J. A.; Johnson, M. S. Clumped Isotope Perturbation in Tropospheric Nitrous Oxide from Stratospheric Photolysis. *Geophys. Res. Lett.* **2015**, *42*, 3546−3552.
(53) Yu, L.; Harris, E.; Lewicka-Szczebak, D.; Barthel, M.; Blomberg, M. R. A.; Harris, S. J.; Johnson, M. S.; Lehmann, M. F.; Liisberg, J.; Müller, C.; Ostrom, N. E.; Six, J.; Toyoda, S.; Yoshida, N.; Mohn, J. What Can We Learn from N_2O Isotope Data? − Analytics, Processes and Modelling. *Rapid Commun. Mass Spectrom.* **2020**, *34*, No. e8858.
(54) Arnoux, P.; Sabaty, M.; Alric, J.; Frangioni, B.; Guigliarelli, B.; Adriano, J.-M.; Pignol, D. Structural and Redox Plasticity in the Heterodimeric Periplasmic Nitrate Reductase. *Nat. Struct. Mol. Biol.* **2003**, *10*, 928−934.
(55) Jormakka, M.; Richardson, D.; Byrne, B.; Iwata, S. Architecture of NarGH Reveals a Structural Classification of Mo-BisMGD Enzymes. *Structure* **2004**, *12*, 95−104.
(56) Scalmani, G.; Frisch, M. J. Continuous Surface Charge Polarizable Continuum Models of Solvation. I. General Formalism. *J. Chem. Phys.* **2010**, *132*, No. 114110.
(57) Marenich, A. V.; Cramer, C. J.; Truhlar, D. G. Universal Solvation Model Based on Solute Electron Density and on a Continuum Model of the Solvent Defined by the Bulk Dielectric Constant and Atomic Surface Tensions. *J. Phys. Chem. B* **2009**, *113*, 6378−6396.
(58) Frisch, M. J.; Trucks, G. W.; Schlegel, H. B.; Scuseria, G. E.; Robb, M. A.; Cheeseman, J. R.; Scalmani, G.; Barone, V.; Mennucci, B.; Petersson, G. A.; Nakatsuji, H.; Caricato, M.; Li, X.; Hratchian, H. P.; Izmaylov, A. F.; Bloino, J.; Zheng, G.; Sonnenberg, J. L.; Hada, M.; Ehara, M.; Toyota, K.; Fukuda, R.; Hasegawa, J.; Ishida, M.; Nakajima, T.; Honda, Y.; Kitao, O.; Nakai, H.; Vreven, T.; Montgomery, J. A., Jr.; Peralta, J. E.; Ogliaro, F.; Bearpark, M.; Heyd, J. J.; Brothers, E.; Kudin, K. N.; Staroverov, V. N.; Kobayashi, R.; Normand, J.; Raghavachari, K.; Rendell, A.; Burant, J. C.; Iyengar, S. S.; Tomasi, J.; Cossi, M.; Rega, N.; Milliam, J. M.; Klene, M.; Knox, J. E.; Cross, J. B.; Bakken, V.; Adamo, C.; Jaramillo, J.; Gomperts, R.; Stratmann, R. E.; Yazyev, O.; Austin, A. J.; Cammi, R.; Pomelli, C.; Ochterski, J. W.; Martin, R. L.; Morokuma, K.; Zakrzewski, V. G.; Voth, G. A.; Salvador, P.; Dannenberg, J. J.; Dapprich, S.; Daniels, A. D.; Farkas, Ö.; Foresman, J. B.; Ortiz, J. V.; Cioslowski, J.; Fox, D. J. *Gaussian 09*; Gaussian, Inc., 2013.
(59) Becke, A. D. Density-functional Thermochemistry. III. The Role of Exact Exchange. *J. Chem. Phys.* **1993**, *98*, 5648−5652.
(60) Lee, C.; Yang, W.; Parr, R. G. Development of the Colle-Salvetti Correlation-Energy Formula into a Functional of the Electron Density. *Phys. Rev. B* **1988**, *37*, 785−789.
(61) Stephens, P. J.; Devlin, F. J.; Chabalowski, C. F.; Frisch, M. J. Ab Initio Calculation of Vibrational Absorption and Circular Dichroism Spectra Using Density Functional Force Fields. *J. Phys. Chem. A* **1994**, *98*, 11623−11627.
(62) Hay, P. J.; Wadt, W. R. *Ab Initio* Effective Core Potentials for Molecular Calculations. Potentials for K to Au Including the Outermost Core Orbitals. *J. Chem. Phys.* **1985**, *82*, 299−310.
(63) Clark, T.; Chandrasekhar, J.; Spitznagel, G. W.; Schleyer, P. V. R. Efficient Diffuse Function-Augmented Basis Sets for Anion Calculations. III. The 3-21+G Basis Set for First-Row Elements, Li-F. *J. Comput. Chem.* **1983**, *4*, 294−301.
(64) Ditchfield, R.; Hehre, W. J.; Pople, J. A. Self-Consistent Molecular-Orbital Methods. IX. An Extended Gaussian-Type Basis for Molecular-Orbital Studies of Organic Molecules. *J. Chem. Phys.* **1971**, *54*, 724−728.
(65) Francl, M. M.; Pietro, W. J.; Hehre, W. J.; Binkley, J. S.; Gordon, M. S.; DeFrees, D. J.; Pople, J. A. Self-consistent Molecular Orbital Methods. XXIII. A Polarization-type Basis Set for Second-row Elements. *J. Chem. Phys.* **1982**, *77*, 3654−3665.
(66) Gordon, M. S.; Binkley, J. S.; Pople, J. A.; Pietro, W. J.; Hehre, W. J. Self-Consistent Molecular-Orbital Methods. 22. Small Split-Valence Basis Sets for Second-Row Elements. *J. Am. Chem. Soc.* **1982**, *104*, 2797−2803.
(67) Hariharan, P. C.; Pople, J. A. The Influence of Polarization Functions on Molecular Orbital Hydrogenation Energies. *Theor. Chim. Acta* **1973**, *28*, 213−222.
(68) Hehre, W. J.; Ditchfield, R.; Pople, J. A. Self—Consistent Molecular Orbital Methods. XII. Further Extensions of Gaussian—Type Basis Sets for Use in Molecular Orbital Studies of Organic Molecules. *J. Chem. Phys.* **1972**, *56*, 2257−2261.
(69) Spitznagel, G. W.; Clark, T.; von Ragué Schleyer, P.; Hehre, W. J. An Evaluation of the Performance of Diffuse Function-Augmented Basis Sets for Second Row Elements, Na-Cl: Diffuse Function-Augmented Basis Sets. *J. Comput. Chem.* **1987**, *8*, 1109−1116.
(70) Bigeleisen, J.; Mayer, M. G. Calculation of Equilibrium Constants for Isotopic Exchange Reactions. *J. Chem. Phys.* **1947**, *15*, 261−267.
(71) Urey, H. C. The Thermodynamic Properties of Isotopic Substances. *J. Chem. Soc.* **1947**, 562.
(72) Melander, L. C. S.; Saunders, W. H. *Reaction Rates of Isotopic Molecules*; Wiley: New York, 1980.
(73) Meija, J.; Coplen, T. B.; Berglund, M.; Brand, W. A.; De Bièvre, P.; Gröning, M.; Holden, N. E.; Irrgeher, J.; Loss, R. D.; Walczyk, T.; Prohaska, T. Isotopic Compositions of the Elements 2013 (IUPAC Technical Report). *Pure Appl. Chem.* **2016**, *88*, 293−306.
(74) Virtanen, P.; Gommers, R.; Oliphant, T. E.; Haberland, M.; Reddy, T.; Cournapeau, D.; Burovski, E.; Peterson, P.; Weckesser, W.; Bright, J.; van der Walt, S. J.; Brett, M.; Wilson, J.; Millman, K. J.; Mayorov, N.; Nelson, A. R. J.; Jones, E.; Kern, R.; Larson, E.; Carey, C. J.; Polat, İ.; Feng, Y.; Moore, E. W.; VanderPlas, J.; Laxalde, D.; Perktold, J.; Cimrman, R.; Henriksen, I.; Quintero, E. A.; Harris, C. R.; Archibald, A. M.; Ribeiro, A. H.; Pedregosa, F.; van Mulbregt, P.; SciPy 1.0 Contributors; Vijaykumar, A.; Bardelli, A. P.; Rothberg, A.; Hilboll, A.; Kloeckner, A.; Scopatz, A.; Lee, A.; Rokem, A.; Woods, C. N.; Fulton, C.; Masson, C.; Häggström, C.; Fitzgerald, C.; Nicholson, D. A.; Hagen, D. R.; Pasechnik, D. V.; Olivetti, E.; Martin, E.; Wieser, E.; Silva, F.; Lenders, F.; Wilhelm, F.; Young, G.; Price, G. A.; Ingold, G.-L.; Allen, G. E.; Lee, G. R.; Audren, H.; Probst, I.; Dietrich, J. P.; Silterra, J.; Webber, J. T.; Slavič, J.; Nothman, J.; Buchner, J.; Kulick, J.; Schönberger, J. L.; de Miranda Cardoso, J. V.; Reimer, J.; Harrington, J.; Rodríguez, J. L. C.; Nunez-Iglesias, J.; Kuczynski, J.; Tritz, K.; Thoma, M.; Newville, M.; Kümmerer, M.; Bolingbroke, M.;

https://doi.org/10.1021/acsearthspacechem.2c00102
ACS Earth Space Chem. 2022, 6, 2582−2594

Tartre, M.; Pak, M.; Smith, N. J.; Nowaczyk, N.; Shebanov, N.; Pavlyk, O.; Brodtkorb, P. A.; Lee, P.; McGibbon, R. T.; Feldbauer, R.; Lewis, S.; Tygier, S.; Sievert, S.; Vigna, S.; Peterson, S.; More, S.; Pudlik, T.; Oshima, T.; Pingel, T. J.; Robitaille, T. P.; Spura, T.; Jones, T. R.; Cera, T.; Leslie, T.; Zito, T.; Krauss, T.; Upadhyay, U.; Halchenko, Y. O.; Vázquez-Baeza, Y. SciPy 1.0: Fundamental Algorithms for Scientific Computing in Python. *Nat. Methods* **2020**, *17*, 261−272.

(75) Xie, H.; Cao, Z. Enzymatic Reduction of Nitrate to Nitrite: Insight from Density Functional Calculations. *Organometallics* **2010**, *29*, 436−441.

(76) Leopoldini, M.; Russo, N.; Toscano, M.; Dulak, M.; Wesolowski, T. A. Mechanism of Nitrate Reduction ByDesulfovibrio Desulfuricans Nitrate Reductase—A Theoretical Investigation. *Chem.—Eur. J.* **2006**, *12*, 2532−2541.

(77) Hofmann, M. Density Functional Theory Studies of Model Complexes for Molybdenum-Dependent Nitrate Reductase Active Sites. *JBIC, J. Biol. Inorg. Chem.* **2007**, *12*, 989−1001.

(78) Hofmann, M. Density Functional Theory Study of Model Complexes for the Revised Nitrate Reductase Active Site in Desulfovibrio Desulfuricans NapA. *JBIC, J. Biol. Inorg. Chem.* **2009**, *14*, 1023.

(79) Fripiat, F.; Martínez-García, A.; Marconi, D.; Fawcett, S. E.; Kopf, S. H.; Luu, V. H.; Rafter, P. A.; Zhang, R.; Sigman, D. M.; Haug, G. H. Nitrogen Isotopic Constraints on Nutrient Transport to the Upper Ocean. *Nat. Geosci.* **2021**, *14*, 855−861.

(80) Whitehill, A. R.; Joelsson, L. M. T.; Schmidt, J. A.; Wang, D. T.; Johnson, M. S.; Ono, S. Clumped Isotope Effects during OH and Cl Oxidation of Methane. *Geochim. Cosmochim. Acta* **2017**, *196*, 307−325.

(81) Eiler, J. M. "Clumped-Isotope" Geochemistry—The Study of Naturally-Occurring, Multiply-Substituted Isotopologues. *Earth Planet. Sci. Lett.* **2007**, *262*, 309−327.

(82) Yeung, L. Y.; Young, E. D.; Schauble, E. A. Measurements of $^{18}O\,^{18}O$ and $^{17}O\,^{18}O$ in the Atmosphere and the Role of Isotope-Exchange Reactions: $^{18}O\,^{18}O$ and $^{17}O\,^{18}O$ in the Atmosphere. *J. Geophys. Res.: Atmos.* **2012**, *117*, No. D18306.

(83) Ash, J. L.; Hu, H.; Yeung, L. Y. What Fractionates Oxygen Isotopes during Respiration? Insights from Multiple Isotopologue Measurements and Theory. *ACS Earth Space Chem.* **2020**, *4*, 50−66.

(84) Eiler, J. M.; Schauble, E. 18O13C16O in Earth's Atmosphere. *Geochim. Cosmochim. Acta* **2004**, *68*, 4767−4777.

(85) Daëron, M.; Guo, W.; Eiler, J.; Genty, D.; Blamart, D.; Boch, R.; Drysdale, R.; Maire, R.; Wainer, K.; Zanchetta, G. 13C18O Clumping in Speleothems: Observations from Natural Caves and Precipitation Experiments. *Geochim. Cosmochim. Acta* **2011**, *75*, 3303−3317.

(86) Guo, W.; Mosenfelder, J. L.; Goddard, W. A.; Eiler, J. M. Isotopic Fractionations Associated with Phosphoric Acid Digestion of Carbonate Minerals: Insights from First-Principles Theoretical Modeling and Clumped Isotope Measurements. *Geochim. Cosmochim. Acta* **2009**, *73*, 7203−7225.

(87) Clog, M.; Lawson, M.; Peterson, B.; Ferreira, A. A.; Santos Neto, E. V.; Eiler, J. M. A Reconnaissance Study of 13C−13C Clumping in Ethane from Natural Gas. *Geochim. Cosmochim. Acta* **2018**, *223*, 229−244.

(88) Douglas, P. M. J.; Stolper, D. A.; Eiler, J. M.; Sessions, A. L.; Lawson, M.; Shuai, Y.; Bishop, A.; Podlaha, O. G.; Ferreira, A. A.; Santos Neto, E. V.; Niemann, M.; Steen, A. S.; Huang, L.; Chimiak, L.; Valentine, D. L.; Fiebig, J.; Luhmann, A. J.; Seyfried, W. E.; Etiope, G.; Schoell, M.; Inskeep, W. P.; Moran, J. J.; Kitchen, N. Methane Clumped Isotopes: Progress and Potential for a New Isotopic Tracer. *Org. Geochem.* **2017**, *113*, 262−282.

(89) Shuai, Y.; Douglas, P. M. J.; Zhang, S.; Stolper, D. A.; Ellis, G. S.; Lawson, M.; Lewan, M. D.; Formolo, M.; Mi, J.; He, K.; Hu, G.; Eiler, J. M. Equilibrium and Non-Equilibrium Controls on the Abundances of Clumped Isotopologues of Methane during Thermogenic Formation in Laboratory Experiments: Implications for the Chemistry of Pyrolysis and the Origins of Natural Gases. *Geochim. Cosmochim. Acta* **2018**, *223*, 159−174.

https://doi.org/10.1021/acsearthspacechem.2c00102
ACS Earth Space Chem. 2022, 6, 2582−2594